




Motion behavior and removal mechanism of inclusions during negative pressure continuous casting process

Qinan Ba^{1,2,3}, Xuefeng Liu^{1,2,3,*} , Yaohua Yang^{2,3,4}, and Wenjing Wang^{2,3}

¹Beijing Advanced Innovation Center for Materials Genome Engineering, University of Science and Technique Beijing, Beijing 100083, China

²Beijing Laboratory of Metallic Materials and Processing for Modern Transportation, University of Science and Technique Beijing, Beijing 100083, China

³Key Laboratory for Advanced Materials Processing of Ministry of Education, University of Science and Technique Beijing, Beijing 100083, China

⁴Shunde Graduate School, University of Science and Technique Beijing, Foshan 528399, Guangdong, China

Received: 22 August 2022

Accepted: 6 November 2022

Published online:

12 November 2022

© The Author(s), under exclusive licence to Springer Science+Business Media, LLC, part of Springer Nature 2022

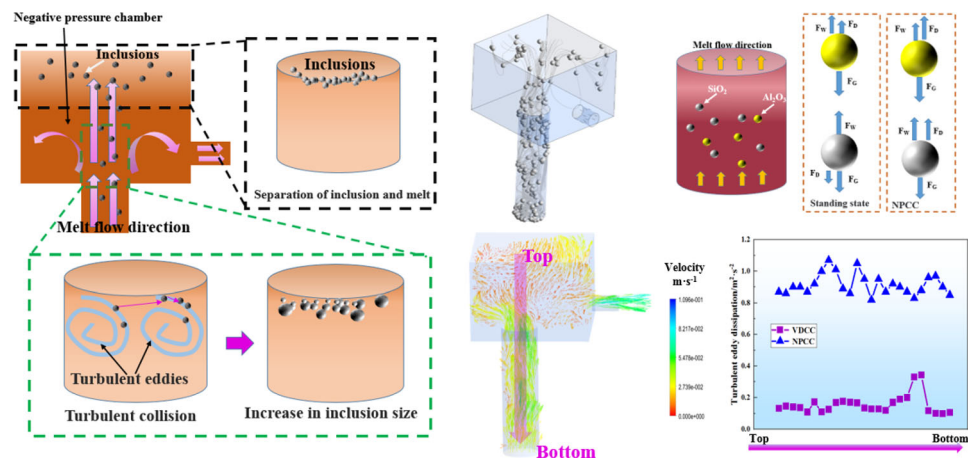
ABSTRACT

The control and removal of inclusions in the continuous casting process can significantly improve the performance of casting billet. In this paper, the aluminum alloy rod billets were prepared by the self-developed negative pressure continuous casting (NPCC) technique. The three-dimensional (3D) morphology and distribution of inclusions in the rod billet were analyzed by X-ray microtomography, the inclusions motion behavior was systematically studied by numerical simulation, and the inclusions removal mechanism was comprehensively revealed. The results show the volume fraction of inclusions in the aluminum alloy rod billet prepared by NPCC technique is 0.03%. Compared with the traditional vertical downward continuous casting (VDCC) technique, the inclusions are reduced by 81.3% and the maximum equivalent diameter is reduced from 24 to 13 μm . By changing the pressure difference inside and outside the melt (PDIOM), NPCC technique makes the melt and inclusions flow in the same direction, which accelerates the floating of inclusions to the melt surface to achieve dynamic solid–liquid separation. Simultaneously, the PDIOM increases the turbulent kinetic energy dissipation rate of melt by a maximum of 44.3 times, and the collision constant of inclusion particles increases by a maximum of 6.7 times. The inclusion particles are more likely to collision and aggregation, which is conducive to the floating and removal of inclusions, thereby further reducing the content and size of inclusions in the rod billet. Overall, this study provides a new continuous casting technique for the preparation of high-quality metal billet with low inclusions content and size.

Handling Editor: Megumi Kawasaki.

Address correspondence to E-mail: liuxuefengbj@163.com

GRAPHICAL ABSTRACT



Introduction

Inclusion is one of the main defects in metal casting billets that is generated during melting, pouring and solidification and is unavoidable during the melting and casting process [1]. Inclusions in the melt exist in the form of particles, films and clusters and are difficult to remove during subsequent hot and cold processing, with a series of subsequent evolutions [2]. Inclusions cause stress concentration between the surrounding substrates, and at the same time, there are microcracks around the inclusions, which adversely affect the strength, toughness, plasticity and fatigue resistance of the metal [3–6]. In addition, the size of inclusions also has a great influence on the performance of the metal billet. The larger the inclusion size is, the greater the local stress concentration caused, and the performance is also reduced. In particular, the inclusions larger than $100\ \mu\text{m}$ have the greatest damage to the quality of the casting billet, which can greatly reduce the performance [7–9]. Hence, it is very important to control the content and size of inclusions in the continuous casting process to improve the quality and performance of the casting billet.

In the process of continuous casting, the separation of inclusions and metal melt is mainly realized by the inclusions motion in the melt, and collision and

aggregation also occur between inclusions during the motion. Different continuous casting techniques have different effects on the inclusions motion, and different casting directions lead to different removal effects of inclusions. During the upward continuous casting process, inclusions are easy to move into the mold in the same direction as the melt, resulting in more inclusions in the metal casting billet [10]. During the horizontal continuous casting process, it is difficult for the inclusions entering the mold to float up and escape [11]. During the vertical downward continuous casting process, the removal effect of inclusions by floating is relatively good, but for the greater density of inclusions is difficult to remove [12]. The traditional continuous casting techniques still suffer from limited removal effect of inclusions and high inclusions content in the casting billet. Therefore, various methods have been developed to assist in the removal of inclusions in metal melt during continuous casting process, such as bubble flotation [13–17], electromagnetic separation [18–22] and other methods. The removal mechanism of inclusions by bubble flotation is that the floating bubbles in the melt continuously collide and adsorb inclusion particles, and the bubbles can also produce turbulent effect and wake during the floating process, increasing the collision probability of inclusions, the inclusions close to the wake area will be involved in

it, so as to achieve the purpose of inclusion removal [17, 23]. Electromagnetic separation mainly uses electromagnetic field to generate pressure difference and forced convection in the melt to control the flow of metal melt, which is conducive to the separation of inclusions and melt [24]. These methods can increase the local flow and turbulent kinetic energy of melt and have different effects on the removal of inclusions in the melt, while they also have certain limitations. The bubble size of the bubble flotation method is difficult to control, and the floating bubbles can only increase the turbulent kinetic energy within the path, and the removal effect of inclusions outside the bubble path is not obvious. A single electromagnetic separation method has a low inclusion removal rate and often needs to be combined with other inclusion removal methods. Therefore, it is of great significance to develop a method to greatly reduce the content and size of inclusions in the casting billet. To sum up, comprehensive consideration of the motion velocity of inclusions, as well as the flow direction and velocity of melt, could be contributed to the separation of inclusions and melt.

Based on the effect of the melt flow direction and velocity on the removal of inclusions, Liu et al. [25] proposed the NPCC technique, by controlling the pressure difference inside and outside the melt, the flow direction and velocity of melt are regulated, which facilitates the separation of inclusions and melt and the reduction of inclusions size in the casting billet.

In this study, the NPCC technique was used to prepare the aluminum alloy rod billet, and the forced flow of melt was induced by regulating the PDIOM, and the turbulent kinetic energy of melt increased. The force of inclusions in the draft tube and the negative pressure chamber was analyzed, the effect of the melt flow direction on the inclusions motion trajectory was studied, and the effect of the turbulent flow on the collision and aggregation of inclusion particles during the NPCC process was explored, and the separation mechanism of inclusions and melt was revealed. This work provides a theoretical basis for the preparation of high-quality metal billets with low inclusions content and size.

Experiment and mathematical model description

Experimental materials and methods

The composition of aluminum alloy used for continuous casting was detected by spectrofluorometry and is shown in Table 1. Aluminum alloy rod billets with a diameter of 10 mm were prepared by VDCC and NPCC techniques, respectively. The melt temperature was 923 K and kept for 20 min, the cooling water temperature of the primary cooling device was set to 300 K, the flow rate was 400 L·h⁻¹, and the continuous casting velocity was 30 mm·min⁻¹. The schematic diagram of NPCC technique is shown in Fig. 1. The aluminum alloy in the crucible was heated and melted by the induction heating coil, and the draft tube and negative pressure chamber were pumped after heat preservation, and the negative pressure value was set to -10 kPa. At this time, the aluminum melt flowed upward into the negative pressure chamber along the draft tube under the action of negative pressure and then flowed into the right casting mold and contacted the dummy bar. The pressure drop velocity was 862 Pa·s⁻¹. The mid-section and the tail section of aluminum alloy continuous casting rod billets were selected for experimental analysis. The mid-section specimen was taken from the rod billet after stable continuous casting, and the tail section specimen was taken from the end of the continuous casting billet, as shown in Fig. 2. The morphology of inclusions was observed, and the composition of inclusions was analyzed by scanning electron microscope (SEM, GeminiSEM500, Carl Zeiss, Germany) with the energy dispersive spectroscopy (EDS). The high-precision X-ray computed microtomography (XCT, FF35CT, YXLON, Germany) was used to observe the inclusion defects in the rod billet, and count the volume fraction and size of the inclusions. A total of 1800 images were acquired every 0.2° with an exposure time of 400 ms. Then, image correction and processing were carried out by YXLON Reconstruction Workspace.

Table 1 Chemical composition of experimental materials (wt%)

Cu	Mn	Fe	Si	Ti	Zn	Mg	Al
0.27	0.11	0.38	0.54	0.016	0.018	0.08	Bal

Figure 1 The schematic diagram of NPCC technique.

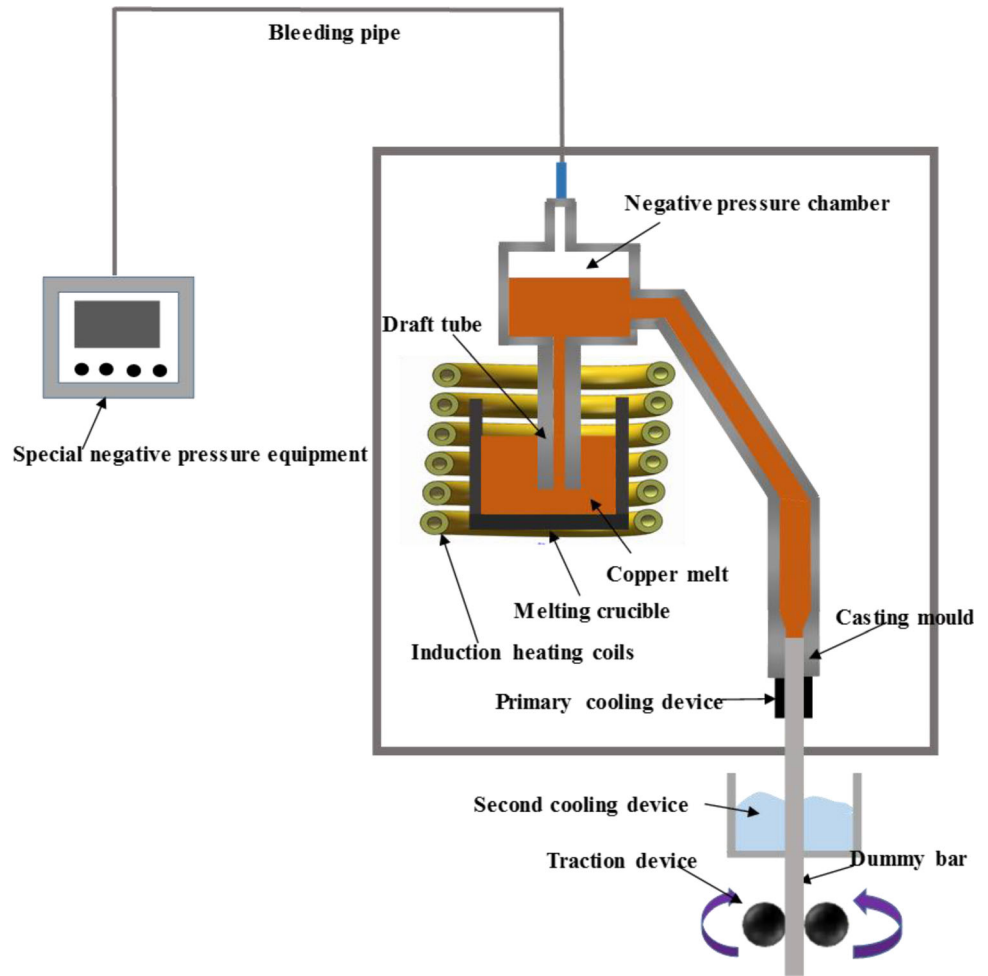
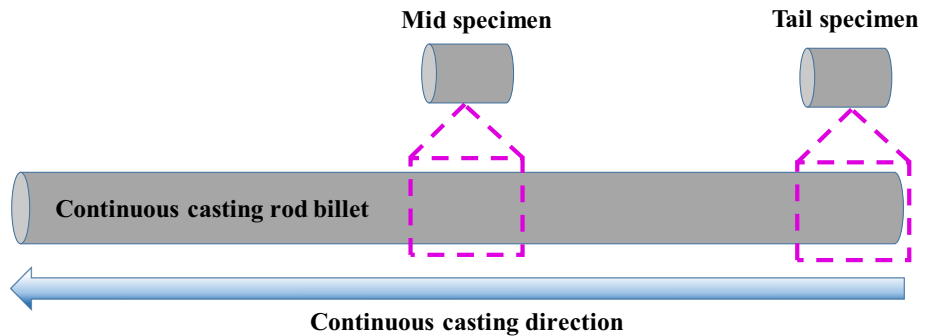


Figure 2 The experimental specimens location.



Finite element numerical simulation and calculation

Figure 3A and c shows the 3D finite element models of aluminum alloy rod billets prepared by NPCC and VDCC, respectively. In order to simplify the calculation, only the crucible was retained in the VDCC, and the draft tube and the negative pressure chamber were retained in the NPCC. Figure 3b and d presents

the meshing of the NPCC and VDCC models, respectively. The physical parameters of the materials in the NPCC and VDCC finite element simulation models are listed in Table 2 [26–28]. The following assumptions were made: (1) the melt was Newtonian viscous fluid and incompressible; (2) the temperature of aluminum alloy melt in the crucible, the draft tube and the negative pressure chamber was uniform; (3) the graphite walls of the crucible, the draft tube and

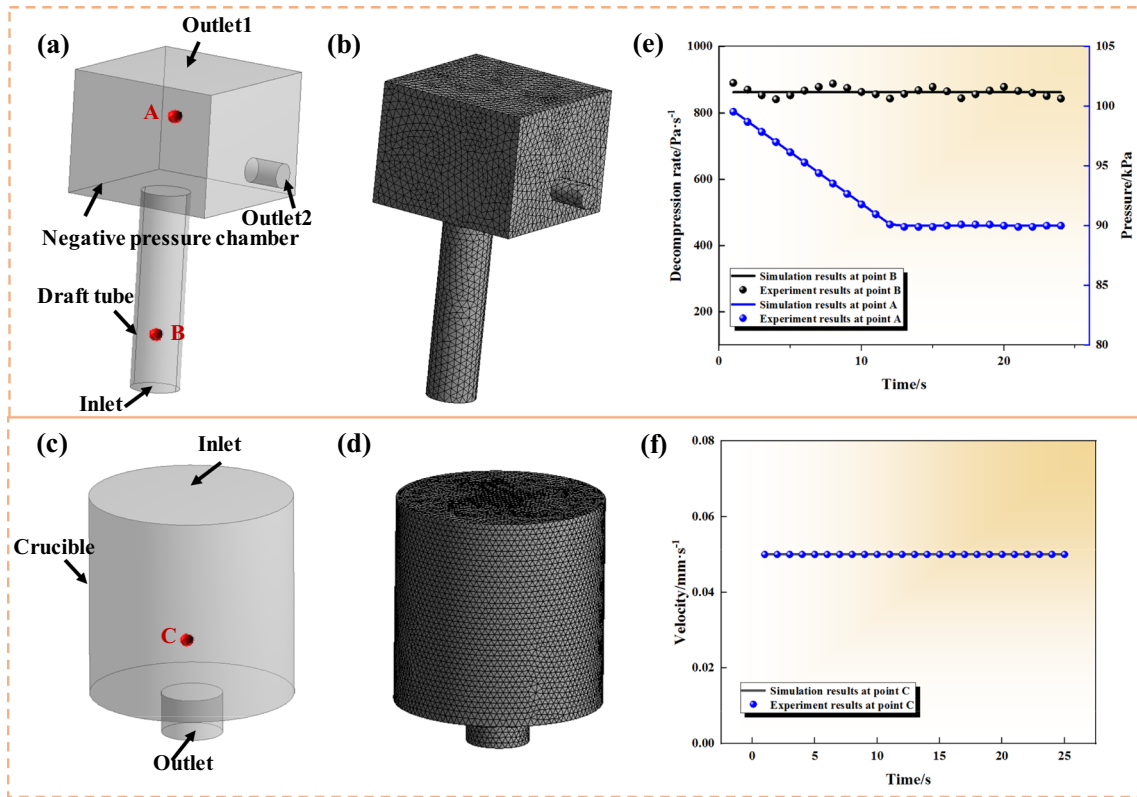


Figure 3 The finite element model of NPCC and VDCC. **a, c** 3D finite element model; **b, d** Mesh; **e** NPCC model validation; **f** VDCC model validation.

Table 2 Physical properties of materials for numerical analysis

Material	Density (kg m ⁻³)	Specific heat (J kg ⁻¹ K ⁻¹)	Thermal conductivity (W·m ⁻² ·K ⁻¹)	Viscosity (kg·m ⁻¹ ·s ⁻¹)	Diameter (μm)
Mold	2250	710	24	–	–
Melt	2700	871	95	0.0013	–
Al ₂ O ₃	3600	771	30	–	1(min)/ 100(max)

the negative pressure chamber were not heat exchange with external environment, which was an adiabatic condition; (4) the influence of electromagnetic force on the melt in actual electromagnetic induction heating was neglected; (5) the inclusion particles were continuous and spherical.

During the continuous casting process, the flow of aluminum alloy melt and inclusions follows the laws of fluid mechanics, and inclusion particles move in the melt as discrete phases, which can be described by the basic governing equations of mass conservation and momentum conservation, involving

turbulent flow, transmission processes such as heat and mass transfer.

In the process of continuous casting, melt and inclusions should satisfy the continuity equation [29, 30]:

$$\nabla \cdot \vec{v} = 0 \tag{1}$$

where \vec{v} is the velocity vector, m s⁻¹.

The fluid flow was considered to be turbulent, using the standard *k*– ϵ model that introduced the turbulent energy dissipation rate ϵ [31]:

$$\frac{\partial(\rho_1 k)}{\partial t} + \frac{\partial(\rho_1 k \mu_t)}{\partial x_i} = \frac{\partial \left[\left(\mu + \frac{\mu_t}{\sigma_k} \right) + \frac{\partial k}{\partial x_j} \right]}{\partial x_j} + G_k - \rho_s \varepsilon \quad (2)$$

$$\frac{\partial(\rho_1 \varepsilon)}{\partial t} + \frac{\partial(\rho_1 \varepsilon \mu_t)}{\partial t} = \frac{\partial \left[\left(\mu + \frac{\mu_t}{\sigma_\varepsilon} \right) + \frac{\partial \varepsilon}{\partial x_j} \right]}{\partial x_j} + C_{1\varepsilon} \frac{\varepsilon}{k} G_k - C_{2\varepsilon} \rho_l \frac{\varepsilon^2}{k} \quad (3)$$

$$\mu_t = C_\mu \rho_l \frac{k^2}{\varepsilon} \quad (4)$$

where t is the time, s , ρ_l is the melt density, $\text{kg}\cdot\text{m}^{-3}$, k is the turbulent energy of the fluid, J , μ_t is the turbulent viscosity coefficient, $\text{Pa}\cdot\text{s}$, G_k is the growth rate of turbulent energy, μ is the molecular viscosity coefficient, $\text{Pa}\cdot\text{s}$, σ_ε and σ_k are turbulent Prandtl numbers for k and ε , $C_{1\varepsilon}$ and $C_{2\varepsilon}$ are the equation constant, C_μ is empirical coefficient, and μ_t is turbulent eddy viscosity, $\text{Pa}\cdot\text{s}$.

The NPCC and VDCC processes included heating and heat transfer processes, which should be calculated by the thermal energy equation for energy conservation [27, 32]:

$$\rho_l \left(\frac{\partial H}{\partial t} + \vec{v} \cdot \nabla H \right) = \nabla(\lambda \nabla H) \quad (5)$$

where λ is the thermal conductivity of pure copper, $\text{W m}^{-2} \text{K}^{-1}$; H is the enthalpy, J .

The motion of inclusion particles during continuous casting was described by the discrete phase model (DPM), and the basic equation could be expressed as [33, 34]:

$$\frac{du_p}{dt} = \frac{3\mu_t C_D Re}{4\rho_p d_p^2} (u - u_p) + \frac{gx(\rho_p - \rho)}{\rho_p} + \frac{1}{2} \frac{\rho}{\rho_p} \frac{d(u - u_p)}{dt} \quad (6)$$

where u_p and u are the velocity of the inclusion particles and melt, respectively, $\text{m}\cdot\text{s}^{-1}$, C_D is the drag coefficient, Re is the relative Reynold number, ρ_p is the inclusion particle density, $\text{kg}\cdot\text{m}^{-3}$, g is the gravitational acceleration, $\text{m}\cdot\text{s}^{-2}$, and d_p is the inclusion particle diameter, m .

For the setting of the NPCC boundary conditions, the inlet and outlet were the velocity inlet and the pressure outlet, respectively, corresponding to the decompression velocity and negative pressure in the actual experiment. The melt temperature and continuous casting velocity were consistent with the experimental parameters. Finally, the governing equations were solved by Fluent software.

The NPCC and VDCC models were validated, as shown in Fig. 3e–f. For the NPCC process, the reduction in pressure was used to pump the melt into the draft tube and negative pressure chamber, so the pressure field and decompressure rate at points A and B were verified, respectively. For the VDCC process, the melt flow rate at point C was verified. The results of the simulations were found to be in good agreement with the experimental results, and both 3D models could be used to simulate both the NPCC and VDCC processes.

Results

Effect of NPCC on inclusions content in aluminum alloy rod billet

Figure 4 shows the 2D distribution and types of inclusions in the aluminum alloy rod billets prepared by NPCC and VDCC. It indicates that the inclusions in the NPCC mid-specimen are very few and almost no inclusions can be observed. However, a higher amount of inclusions can be observed in the NPCC tail specimen, as displayed in Fig. 4a and c. A small amount of inclusions can be found in the VDCC mid-specimen, which has a higher amount of inclusions than that of NPCC, as displayed in Fig. 4b. The amount of inclusions in the VDCC tail specimen increases more than that in the VDCC mid-specimen, as shown in Fig. 4d. In addition, the inclusions content in the NPCC tail specimen is higher than that in the VDCC tail specimen. The types of inclusions are mainly Al_2O_3 and a small amount of SiO_2 and Fe-rich impurity phase, which have higher melting points, as presented in Fig. 4e.

In order to further observe the morphology and content of inclusions in the aluminum alloy rod billets prepared by NPCC and VDCC, the 3D morphology of inclusions was observed by X-ray microtomography and the volume fraction was calculated, as shown in Fig. 5. It can be seen that the inclusions in the NPCC mid-specimen are less and smaller in size, with an inclusions volume fraction of 0.03%, as shown in Fig. 5a. In the mid-specimen of VDCC, the content of inclusions increases, and a small amount of inclusions occurs segregation, with the volume fraction of 0.16% for inclusions, as displayed in Fig. 5b. In contrast, larger size and more numerous inclusions are observed in the NPCC tail

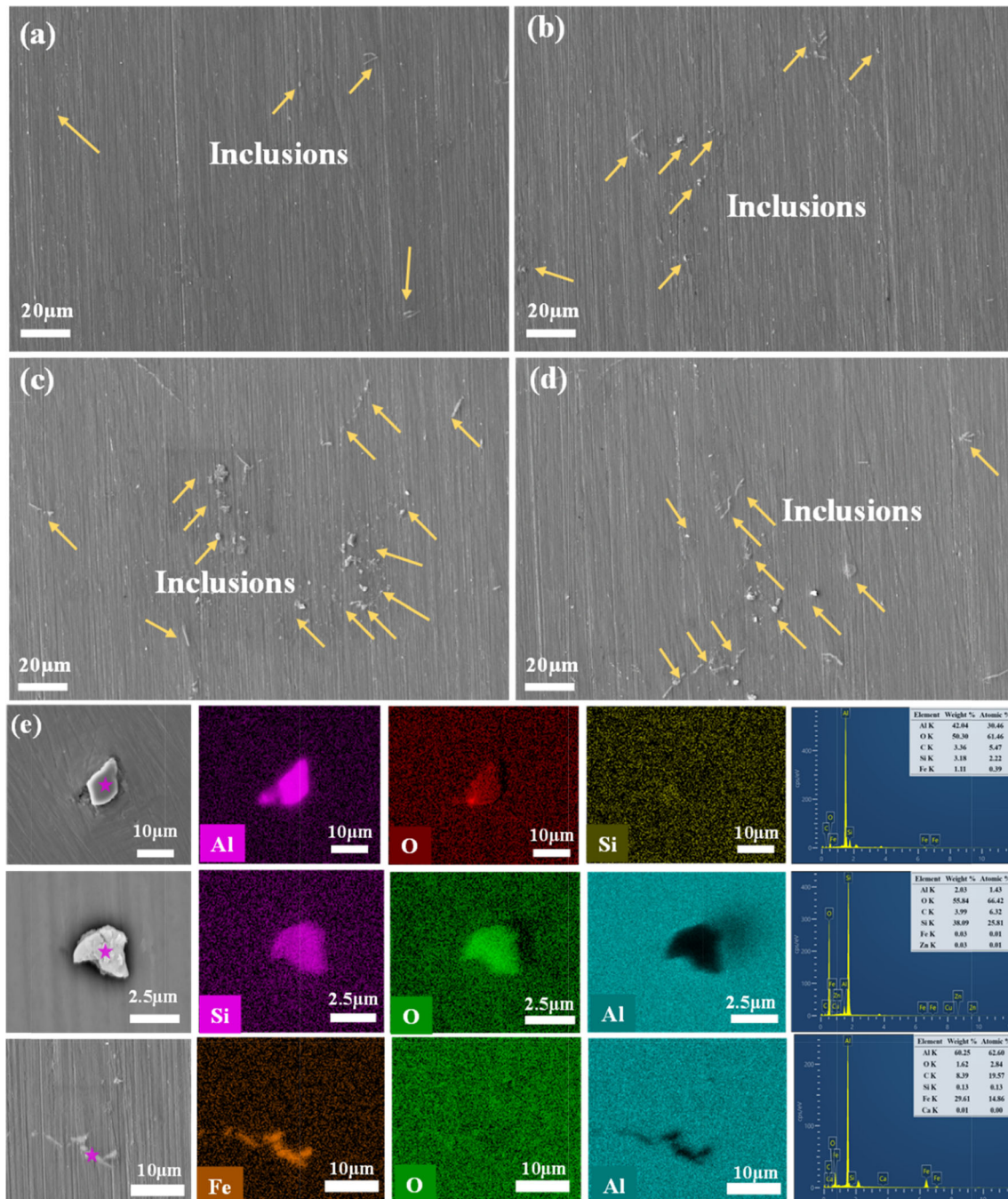


Figure 4 SEM images of inclusion defects in aluminum alloy rod billets under different processes. **a** NPCC mid-specimen; **b** VDCC mid-specimen; **c** NPCC tail specimen; **d** VDCC tail specimen; **e** typical inclusions.

specimen, with an inclusion volume fraction of 0.8%, as shown in Fig. 5c. Larger size and more numerous inclusions are also found in the VDCC tail specimen, with a volume fraction of 0.4%, as shown in Fig. 5d. Compared with the mid-specimen of the aluminum alloy rod billet, the inclusions size in the tail specimen is larger as well as more numerous. Moreover, the

inclusions content in the NPCC mid-specimen is less compared to the VDCC mid-specimen, while the inclusions content in the NPCC tail specimen is more, as presented in Fig. 5e. In conclusion, the NPCC technique is contributed to remove the inclusions in the mid-specimen of the aluminum alloy rod billet, so that the inclusions are separated from the melt, and

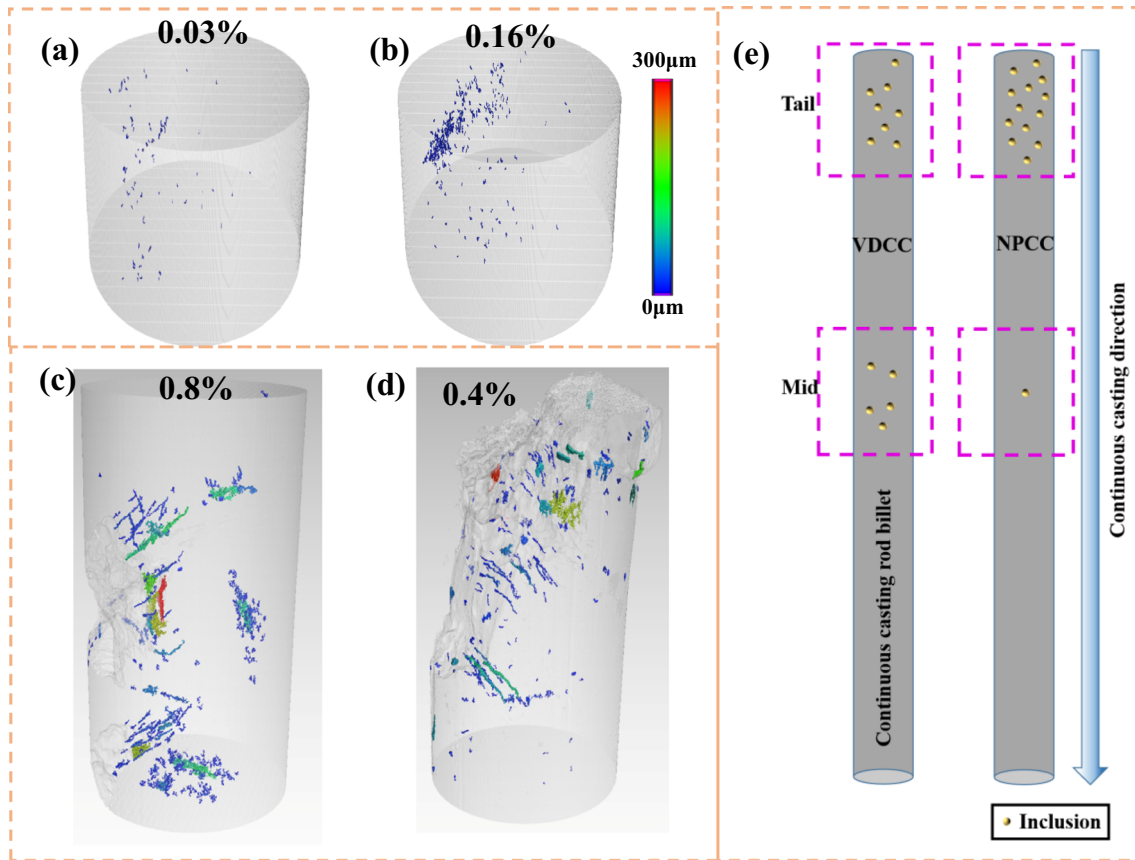


Figure 5 XCT images of inclusion defects in aluminum alloy rod billets under different continuous casting processes. **a** NPCC mid-specimen; **b** VDCC mid-specimen; **c** NPCC tail specimen; **d** VDCC tail specimen; **e** schematic diagram of the inclusions distribution.

the inclusions are mainly concentrated in the tail of the rod billet.

Effect of NPCC on inclusions size in aluminum alloy rod billet

The relationship between the equivalent diameter and sphericity of inclusions in the mid and tail specimens of NPCC and VDCC is shown in Fig. 6, and the data were extracted from Fig. 5. It can be found that the equivalent diameter of inclusions is approximately inversely proportional to the sphericity. The larger the equivalent diameter, the more irregular the inclusions, and the smaller the sphericity. The equivalent diameter of inclusions in the NPCC mid-specimen is mainly distributed between 0 and 10 μm , and the sphericity is mainly concentrated between 0.42 and 0.58. There are also a small amount of inclusions that equivalent diameter is distributed between 10 and 13 μm , sphericity is mainly concentrated between 0.40 and 0.45, and the probability is 5.2%, as shown in Figs. 6a and 7a. Nevertheless, the

equivalent diameter of inclusions in the NPCC tail specimen is mainly distributed between 0 and 100 μm , and the sphericity is mainly between 0.13 and 0.48. A small amount of inclusions that equivalent diameter is distributed between 100 and 300 μm , sphericity is mainly between 0.09 and 0.25, and the probability is 10.4%, as displayed in Figs. 6c and 7c. Compared with the NPCC mid-specimen, the equivalent diameter of inclusions in the VDCC mid-specimen increases, mainly distributed between 0 and 15 μm , and the sphericity is mainly between 0.34 and 0.62. A small amount of inclusions that equivalent diameter is distributed between 15 and 25 μm and sphericity is between 0.31 and 0.45, and the probability of equivalent diameter larger than 10 μm increases to 20.2%, as shown in Figs. 6b and 7b. The inclusions size is larger than that in the NPCC mid-specimen. The inclusions content in the VDCC tail specimen decreases compared to the NPCC tail specimen. The equivalent diameter of inclusions is mainly distributed between 0 and 100 μm , and the

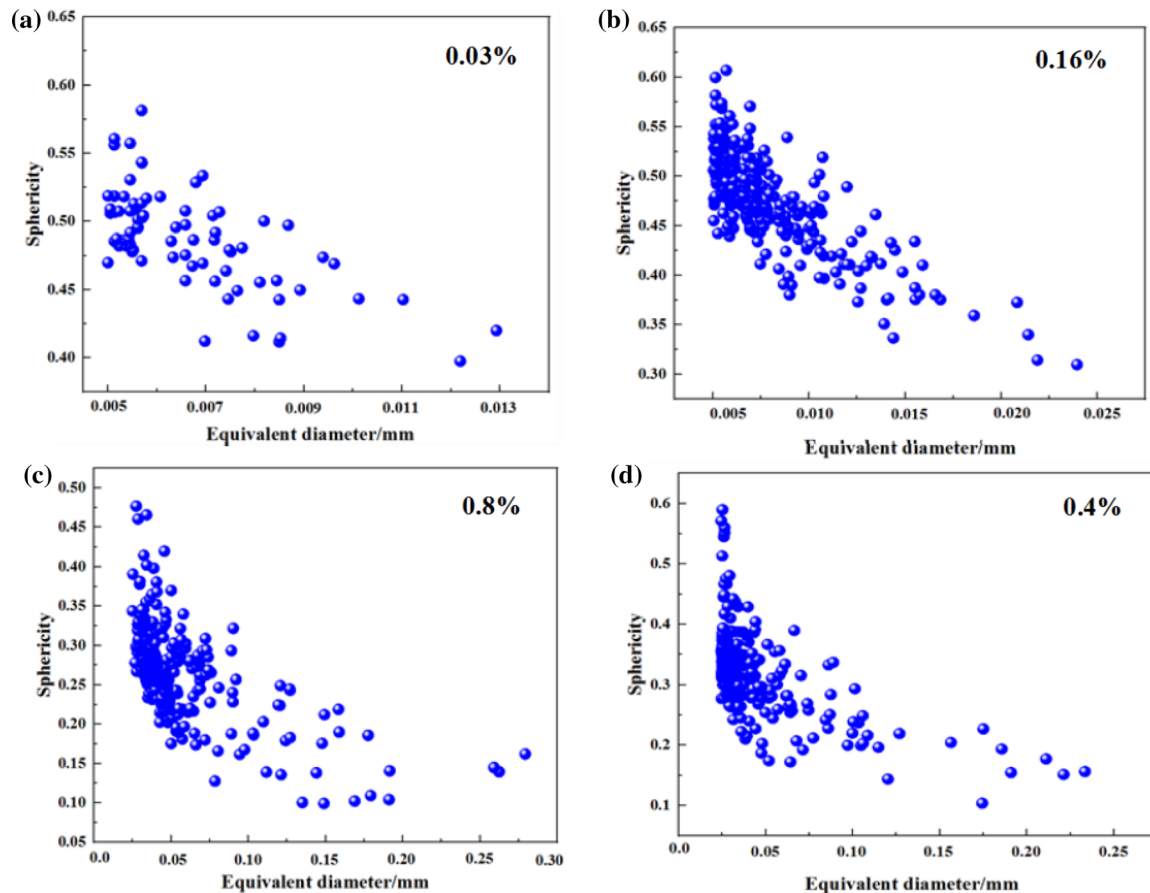


Figure 6 The relationship between the equivalent diameter and sphericity of inclusions under different continuous casting processes. **a** NPCC mid-specimen; **b** VDCC mid-specimen; **c** NPCC tail specimen; **d** VDCC tail specimen.

sphericity is between 0.17 and 0.60. A small amount of inclusions is distributed between 100 and 250 μm , the sphericity is between 0.10 and 0.30, and the probability is 8.0%, as presented in Figs. 6d and 7d. The content and size of inclusions in the NPCC mid-specimen are lower than that in the VDCC mid-specimen, and the sphericity distribution range of inclusions in the VDCC mid-specimen is larger. In contrast, the content and size of inclusions in the VDCC tail specimen are lower than that in the NPCC tail specimen, and the inclusions have relatively higher sphericity and more regular shapes. The NPCC technique is conducive to the floating removal of inclusions, reducing the inclusions content and equivalent diameter in the mid-section of the aluminum alloy rod billet. As a consequence, more and larger inclusions are concentrated in the tail of the aluminum alloy rod billet.

Discussion

Effect of the resting process on the inclusions motion

During the NPCC holding process, the inclusion particles undergo floating and settling motions during the resting time (20 min), as shown in Fig. 8c. The floating or settling rate of inclusions of different radius sizes in a static melt can be calculated using the Stokes velocity equation [35]:

$$u_p = \frac{2(\rho - \rho_p)gr^2}{9\rho\mu} \quad (7)$$

where r is the radius of the inclusion particle, m.

According to Eq. 7, the floating and settling velocities of the inclusion particles with different radii and the motion distance after 20 min can be derived, as shown in Fig. 8a and b. It can be found that the larger the radius of the inclusion particles, the greater the floating or settling rate. After 20 min

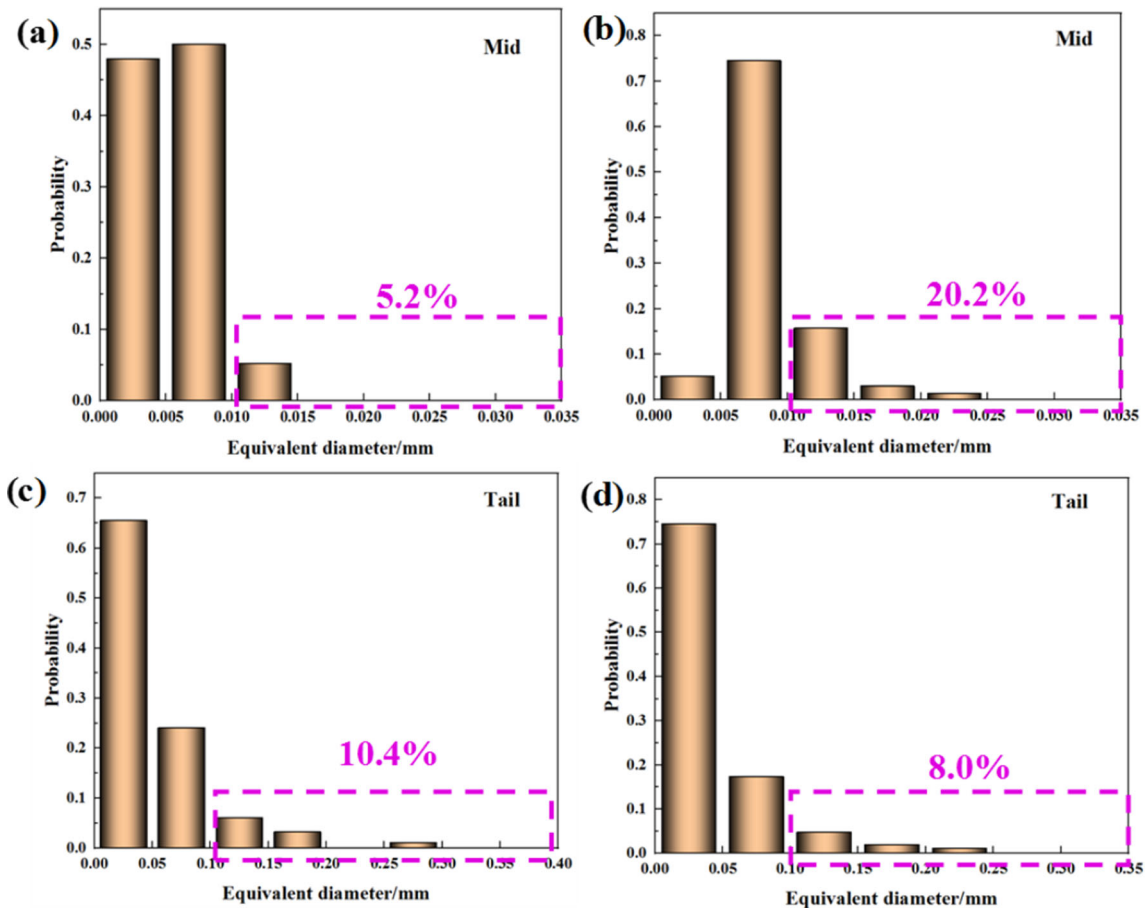


Figure 7 Equivalent diameter probability distribution of inclusions under different continuous casting processes. **a** NPCC mid-specimen; **b** VDCC mid-specimen; **c** NPCC tail specimen; **d** VDCC tail specimen.

of resting, Al_2O_3 particles with a radius greater than $152\ \mu m$ and SiO_2 particles with a radius greater than $279\ \mu m$ settle and float over a distance greater than the melt depth (100 mm), and this part of inclusion particles float to the melt surface or settle to the bottom of melt. However, the radii of inclusion particles in different melt depths vary, as do the velocity and distance of movement. For Al_2O_3 particles, the smaller the melt depth, the larger the radius of particles required to settle to the bottom of the melt. For SiO_2 particles, the greater the melt depth, the greater the radius of particles required to float to the melt surface, as shown in Fig. 8d. Anyway, during the resting process of NPCC and VDCC, Al_2O_3 and SiO_2 particles of different sizes in different melt depths will undergo floating and settling processes, and the particles larger than the critical radius will settle to the bottom of melt and float to the melt surface, thus achieving the separation of the inclusion particles from the melt. Nevertheless, during the VDCC

process, the Al_2O_3 particles that settle toward the bottom of melt tend to enter the mold and are trapped in the solid phase to form inclusion defects, which can lead to an increase in inclusions in the rod billets. The NPCC process avoids this part of inclusion particles from entering the mold directly due to the presence of the draft tube and negative pressure chamber. This is one reason why the inclusions in VDCC mid-specimen are higher than those in NPCC mid-specimen (Fig. 5a–b).

Effect of the melt flow direction on the inclusions motion

As we know, inclusions with larger size move faster during the resting process and easily float to the melt surface or settle to the melt bottom to achieve separation from the melt. However, inclusions with small size (diameter $\leq 100\ \mu m$) move very slowly, as shown in Figs. 8a and b. Hence, the removal of

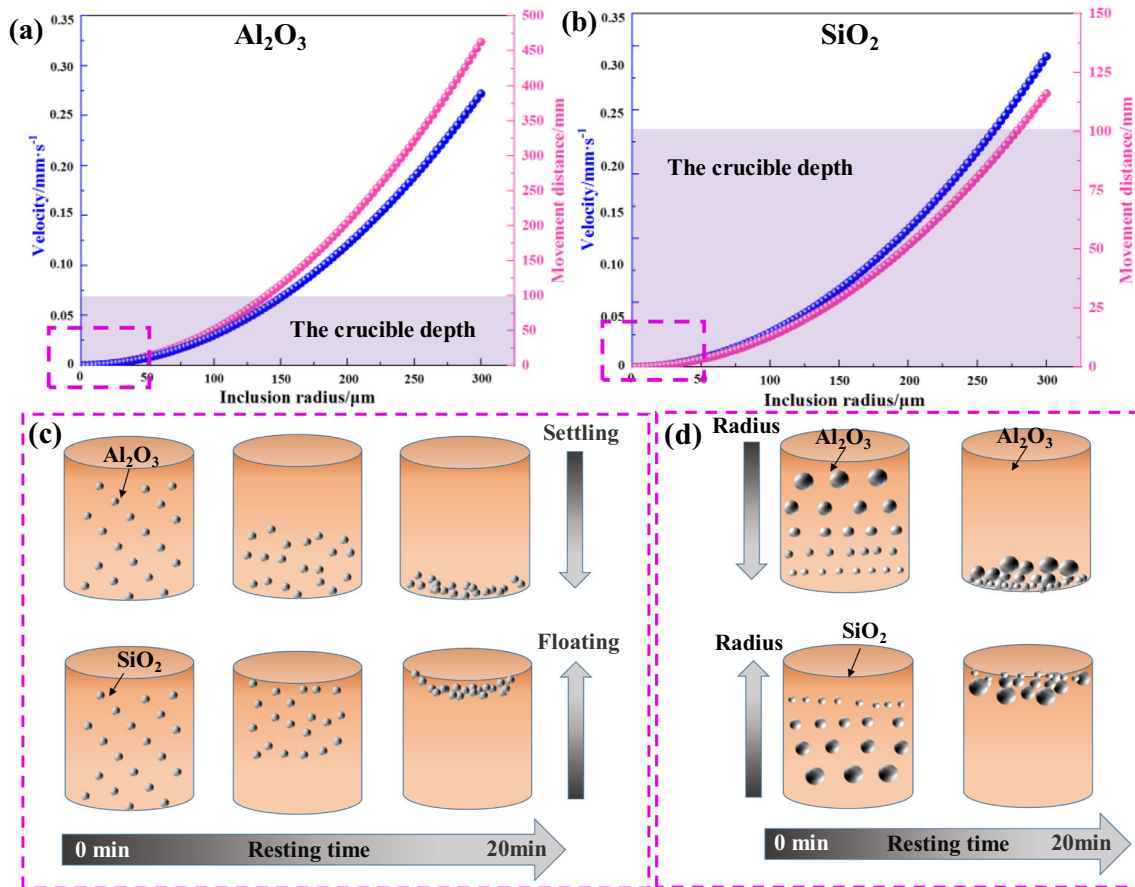


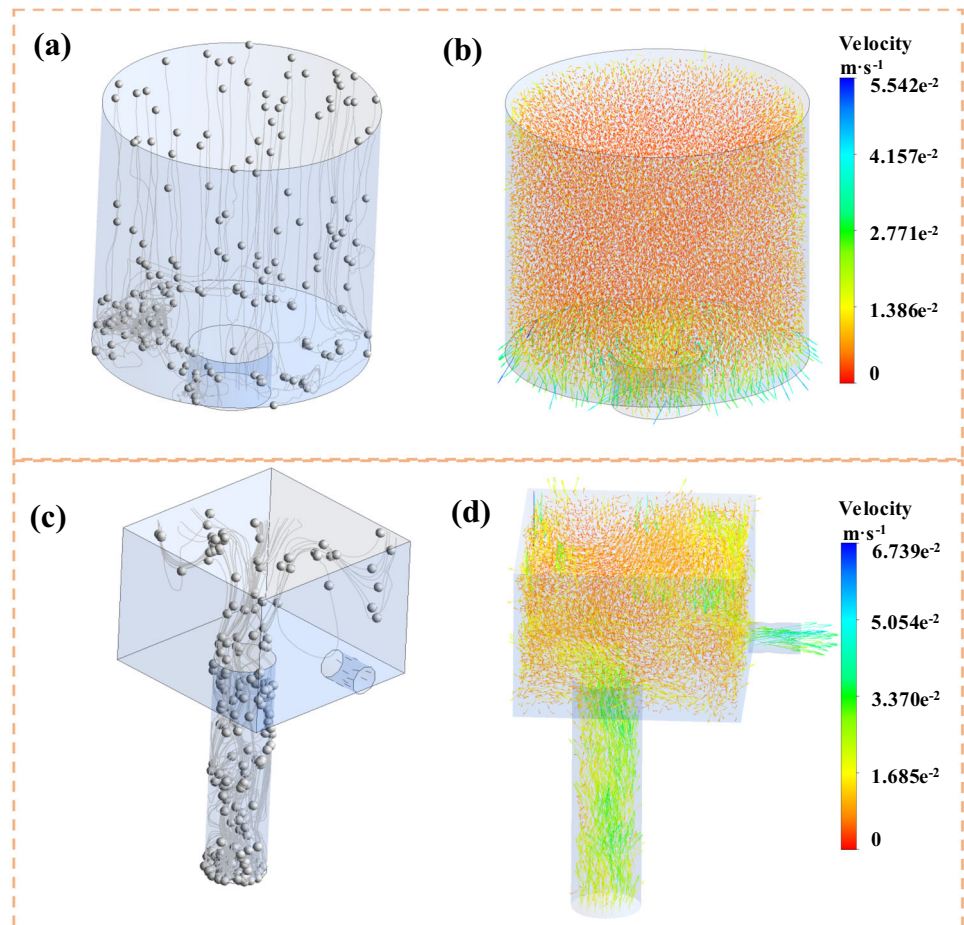
Figure 8 Movement of inclusion particles during resting process. **a** Al_2O_3 particle settling velocity and motion distance; **b** SiO_2 particle settling velocity and motion distance; **c** schematic diagram

of the floating and settling process of inclusion particles; **d** schematic diagram of the floating and settling processes of different inclusion particles sizes in different depths.

inclusions with the diameter of less than 100 μm in the melt is particularly important for improving the quality of the casting billet. Based on the above experimental results, it indicates that the NPCC technique has a better effect on the removal of inclusions. Regarding the inclusion removal mechanism of NPCC technique, it is first necessary to reveal the effect of the melt flow direction caused by the PDIOM on the inclusions motion during the NPCC process. Numerical simulations of the motion trajectories of inclusion particles during NPCC and VDCC processes were performed, as shown in Fig. 9. Since the main inclusion in the aluminum alloy rod billet is Al_2O_3 , the Al_2O_3 particles were used in the numerical simulation, and the particles diameter was 1–100 μm . The melt flow in VDCC is the turbulent motion, the flow is relatively uniform, and the overall velocity vector direction is downward, as displayed in Fig. 9b. The Al_2O_3 particles are mainly concentrated in the

bottom of the crucible, and some Al_2O_3 particles move toward the mold under the influence of the gravity and the melt flow and gradually flow into the mold with the melt, as presented in Fig. 9a. The velocity vector of the melt flow in the draft tube is mainly upward. Compared with VDCC, the flow velocity increases, and the Al_2O_3 particles are greatly affected by the melt flow direction, and flow upward into the negative pressure chamber with the melt. The inclusions entering the negative pressure chamber have the jet effect, resulting in a large upward velocity vector, which is less affected by the horizontal flow velocity. Therefore, the inclusion particles hardly enter the horizontal flow channel and are mainly concentrated in the upper part of the negative pressure chamber, as shown in Fig. 9c and d. In summary, VDCC has limited effect on the separation of melt and inclusion particles, resulting in a higher inclusions content in the mid-section of the rod billet

Figure 9 Motion trajectories of inclusion particles in different continuous casting processes. **a** Motion trajectories of inclusion particles in VDCC; **b** velocity vector distribution in VDCC; **c** motion trajectories of inclusion particles in NPCC; **d** velocity vector distribution in NPCC.



than that of NPCC (Figs. 4a–b and 5a–b). In the NPCC process, the dynamic separation of inclusion particles and melt is realized in the negative pressure chamber, which greatly reduces the content of inclusions entering the mold, resulting in a reduction in the content of inclusions in the mid-section of the rod billet and making it mainly distribute in the tail section, the inclusions content of the tail section increases, as shown in Fig. 5c–d.

Inclusion particles in the melt are mainly affected by gravity F_G , buoyancy F_W and drag force F_D during the resting process, and the virtual mass force and pressure gradient force are ignored. During the VDCC process, the melt flow direction is consistent with the continuous casting direction, as displayed in Fig. 10a. The force on the inclusion particles is shown in Fig. 10b. For inclusions with a density greater than melt (Al_2O_3), F_G plays a dominant role, and the motion direction of inclusions is consistent with the melt flow direction and the continuous casting direction. At this point, the F_D direction received by

smaller size Al_2O_3 particle with settlement velocity less than melt flow velocity changes from opposite to same as F_G . The larger size Al_2O_3 particle with a settlement velocity greater than the melt flow velocity receives a smaller F_D and a faster settlement velocity, which is easier to flow into the mold and form inclusion defects in the rod billet. During the NPCC process, the melt flow direction in the draft tube and the negative pressure chamber is opposite to the continuous casting direction, as shown in Fig. 10c. The PDIOM causes the forced flow of melt, changes the melt flow direction and the force of the inclusion particles in the draft tube and the negative pressure chamber, as shown in Fig. 10d. The PDIOM causes the melt flow velocity to be larger, which leads to the change of F_D received by the Al_2O_3 particles, making the Al_2O_3 particles flow in the same direction to the melt surface in the negative pressure chamber. In addition, the melt flow direction also has an effect on the motion of inclusions (SiO_2) with a density less than melt. During the VDCC process, the motion of

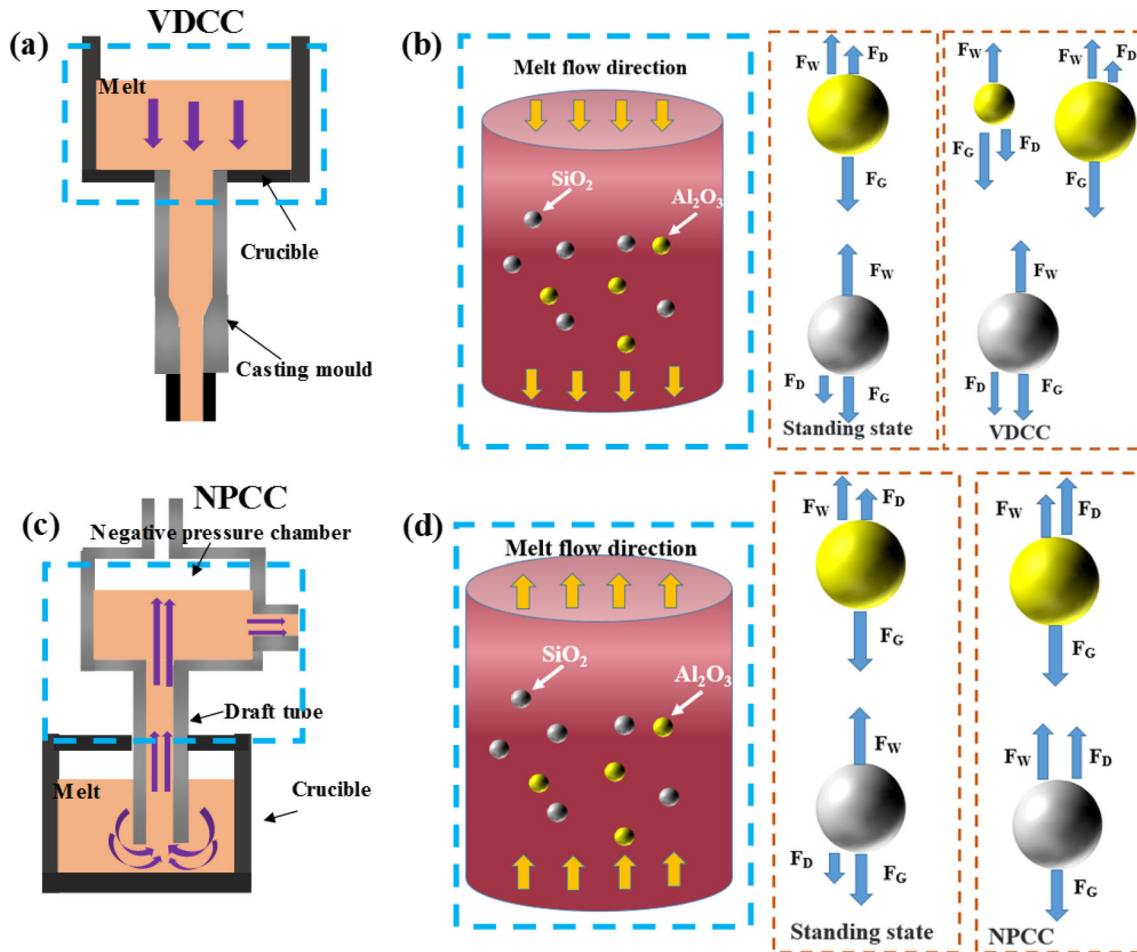


Figure 10 Schematic diagram of the force on the inclusion particles. **a** Melt flow in VDCC process; **b** the force on the inclusion particles in VDCC process; **c** melt flow in NPCC process; **d** the force on the inclusion particles in NPCC process.

SiO_2 particles is dominated by F_W , and the motion direction is opposite to the melt flow direction, which leads to an increase in the F_W of inclusions, which is not conducive to the floating of SiO_2 . In the NPCC process, the direction and magnitude of F_D subjected by SiO_2 particles change, and the motion direction is the same as the melt flow direction, and the floating process is accelerated. Therefore, the NPCC technique has obvious effect on the removal of inclusions in the melt.

Effect of melt turbulence on the collisional aggregation of inclusion particles

In the continuous casting process, the melt flows in a turbulent manner, and turbulent collision occurs between inclusion particles in the melt [36, 37]. When the inclusion particles move in the turbulent melt, under the effect of the turbulent eddies, the

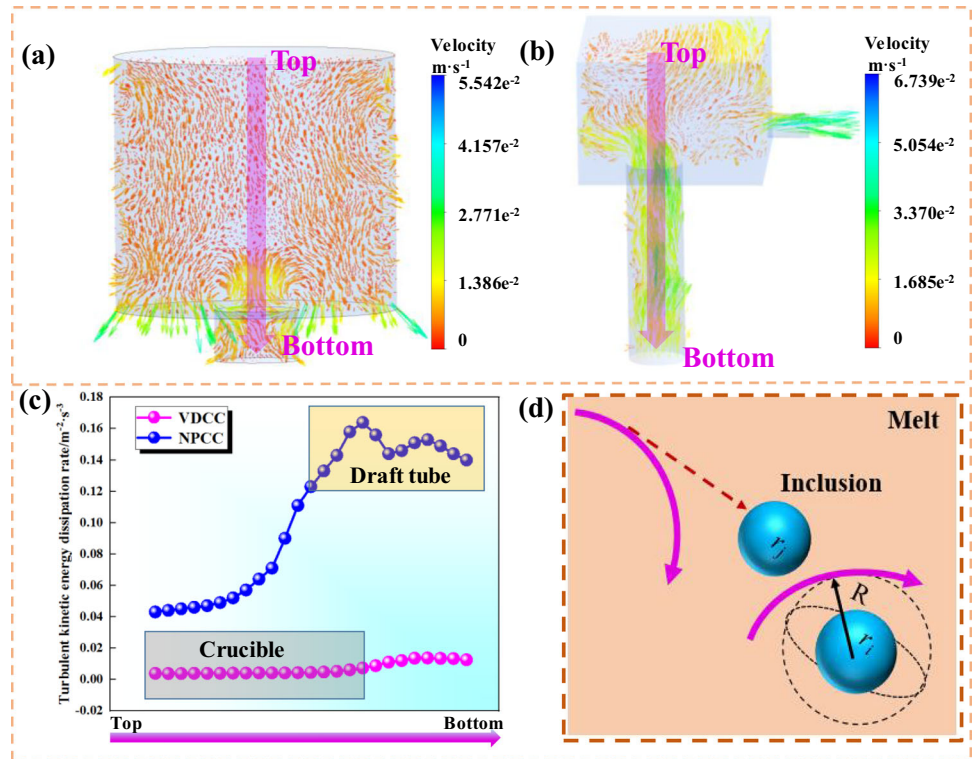
inclusions collide and aggregate, then larger inclusions are formed, as displayed in Fig. 11d. Inclusions with larger sizes float or settle faster, making it easier to achieve separation from the melt. The collision between inclusions is related to the turbulent kinetic energy dissipation rate ε of the melt, and the collision constant β_s can be calculated as [38, 39]:

$$\beta_s = 1.3(r_i + r_j)^3 \sqrt{\frac{\rho\varepsilon}{\mu}} \quad (8)$$

where r_i and r_j are the radius of the inclusion particle in group i and j , respectively.

According to Eq. 8, the larger the turbulent kinetic energy dissipation rate, the larger the collision constant of the inclusion particles. Figure 11a and b presents the velocity field distributions of the melt longitudinal section in VDCC and NPCC, respectively. It can be found that during the VDCC process, the melt flow is relatively slow and stable, and the

Figure 11 Turbulent collision of inclusions in the melt under different continuous casting processes. **a** The velocity field distribution of melt longitudinal section in VDCC; **b** the velocity field distribution of melt longitudinal section in NPCC; **c** statistics of turbulent kinetic energy dissipation rate in different positions; **d** schematic diagram of turbulent collision of inclusion particles.



fluctuation of the local turbulent flow is small, and the melt flow velocity increases significantly only in the mold; during the NPCC process, the turbulent kinetic energy increases due to the greater melt flow velocity. Statistics of the turbulent kinetic energy dissipation rate of the melt from top to bottom under the two processes (indicated by the pink arrows in Fig. 11a–b) are shown in Fig. 11c. It indicates that the turbulent kinetic energy dissipation rate of NPCC is 3.16–44.3 times higher than that of VDCC, and the collision constant is 1.8–6.7 times higher than that of VDCC. In particular, the rate of turbulent energy dissipation is greatest in the draft tube. This is due to the PDIOM, and the melt in the draft tube and the negative pressure chamber follows the Bernoulli equation [40, 41].

$$\frac{\rho_1 v^2}{2} + \rho_1 g z + P = C \tag{9}$$

where P is the pressure of the selected point, Pa, z is the height of the point on the reference plane, m, and C is a constant.

When the external pressure of melt decreases, the melt accelerates into the draft tube under the action of the negative pressure difference, and then flows into the negative pressure chamber. The increase of the melt flow velocity leads to an increase of the local

turbulent kinetic energy, which in turn increases the turbulent kinetic energy dissipation rate, as the Reference [42] reported. Therefore, the collision constant of the inclusion particles in NPCC is larger, and the collision and aggregation between inclusion particles are more likely to occur, and the larger sized inclusions float to the melt surface in the negative pressure chamber, thus achieving the separation from the melt. When the initial content and size of inclusions in the melt in VDCC and NPCC are the same, more inclusions in the melt in NPCC have turbulent collisions to form larger sized inclusions. The size of inclusions floating up to the negative pressure chamber is larger than the size of inclusions on the melt surface in VDCC. Therefore, the size of inclusions in the NPCC mid-specimen is smaller than that in the VDCC mid-specimen, while the size of inclusions in the NPCC tail specimen is larger than that in the VDCC tail specimen, as displayed in Figs. 6 and 7.

In summary, NPCC establishes the pressure difference inside and outside the melt in the crucible, and uses the pressure difference to cause the melt to flow, changing the melt flow direction, so that the melt and inclusions flow into the draft tube in the same direction, and dynamic solid–liquid separation is realized in the negative pressure chamber.

Simultaneously, the existence of the PDIOM can increase the local turbulent kinetic energy dissipation rate of the melt in the draft tube and the negative pressure chamber, which in turn increases the probability of collision and aggregation of inclusions, which is conducive to the growth and removal of inclusions, and the content and size of inclusions in the rod billet could be reduced, as shown in Fig. 12.

Conclusions

- (1) The volume fraction of inclusions in the aluminum alloy rod billet prepared by NPCC technique is 0.03%. Compared with the traditional VDCC technique, the inclusions are reduced by 81.3%, and the size of inclusions is significantly reduced, the maximum equivalent diameter is reduced from 24 to 13 μm , the inclusions with an equivalent radius greater than 10 μm are reduced by 15%, and the NPCC technique effectively reduces the inclusions in the aluminum alloy rod billet.
- (2) The NPCC technique avoids the inclusion particles from entering the mold directly in the resting process. NPCC causes the PDIOM, which forces the melt to flow, changes the melt flow direction, and makes the melt and

inclusions flow in the same direction in the draft tube. The resistance to the floating of inclusions is reduced, so that the inclusions accelerate to the melt surface in the negative pressure chamber, to achieve the dynamic solid–liquid separation of the inclusion particles and the melt in the negative pressure chamber.

- (3) During the NPCC process, the PDIOM increases the turbulent kinetic energy dissipation rate of the melt by a maximum of 44.3 times and increases the collision constant of inclusion particles by a maximum of 6.7 times. It is easier to collide and aggregate between the inclusion particles, and the formed inclusions with larger sizes are more likely to float up to the melt surface in the negative pressure chamber, thereby achieving separation from the melt.
- (4) The NPCC technique regulates the direction and velocity of melt flow by controlling the PDIOM, which is the fundamental reason for reducing the content and size of inclusions in the continuous casting rod billet.

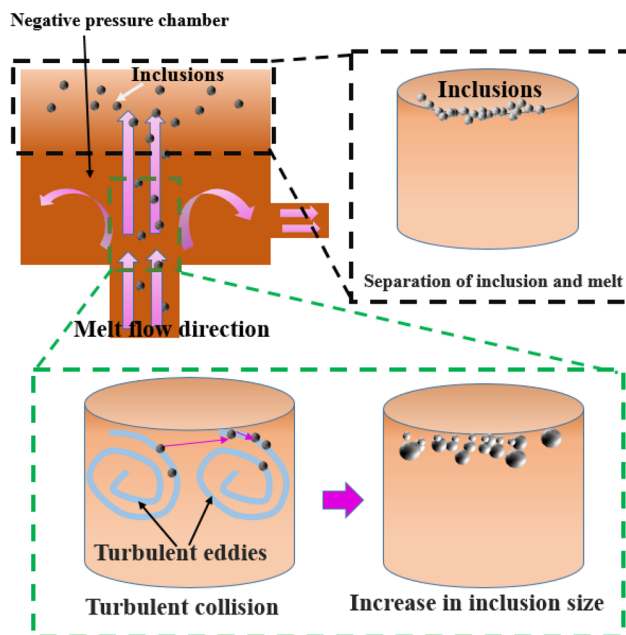


Figure 12 Schematic diagram of the inclusion removal mechanism of NPCC technique.

Acknowledgements

This work was supported by the National Natural Science Foundation of China (51974027, U1703131) and the Guangdong Basic and Applied Basic Research Foundation (2019A151511126).

Declarations

Conflict of interest We declare that all authors have no conflict of interest.

References

- [1] Shannon G, White L, Sridhar S (2008) Modeling inclusion approach to the steel/slag interface. *Mat Sci Eng A* 495:310–315
- [2] Wang F, Fan ZY (2019) Characterization of AlN inclusion particles formed in commercial purity aluminum. *Metall Mater Trans A* 50:2519–2526
- [3] Rajput A, Paul SK (2021) Effect of soft and hard inclusions in tensile deformation and damage mechanism of aluminum: a molecular dynamics study. *J Alloy Compd* 869:159213

- [4] Zheng LC, Malfiet A, Wollants P, Blanpain B, Guo MX (2016) Effect of alumina morphology on the clustering of alumina inclusions in molten iron. *ISIJ Int* 56:926–935
- [5] Seleznev M, Henschel S, Storti E, Aneziris CG, Krüger L, Weidner A, Biermann H (2020) Effect of filter functional coating on detrimental nonmetallic inclusions in 42CrMo4 steel and its resulting mechanical properties. *Adv Eng Mat* 22:1900540
- [6] Li LY, Cheng GG, Hu B, Wang CS, Qian G (2018) Formation of non-metallic inclusions of Si-killed stainless steel during GOR refining process. *High Temp Mat Process* 37:521–529
- [7] Emi T (1975) Origin and removal of large non-metallic inclusions in steel[J]. *Scand J Metall* 4:1–8
- [8] Li H, Zhao D, Zhu G, Bao CL, Yang J (2015) Influence of inclusions on impact properties of J55 steel. *J Iron Steel Res Int* 22:36–41
- [9] Zheng L, Zhang GQ, Gorley MJ, Lee TL, Li Z, Xiao CB, Tang CC (2021) Effects of vacuum on gas content, oxide inclusions and mechanical properties of Ni-based superalloy using electron beam button and synchrotron diffraction. *Mater Des* 207:109861
- [10] Yuan DW, Chen JS, Xiao XP, Han BJ, Huang H, Liu BX, Yang B (2021) Microstructure and properties of Cu-Fe-Cr-Ag alloy prepared by directional solidification and upward continuous casting. *Metall Mater Trans A* 52:2489–2500
- [11] You BS, Yim CD, Kim SH (2005) Solidification of AZ31 magnesium alloy plate in a horizontal continuous casting process. *Mat Sci Eng A* 413:139–143
- [12] Zhang LW, Wang ZL, Xu CJ, Li SL, Ai XG, Li Z (2019) A vertical continuous casting machine for large blooms. *Iron Steel* 46(08):742–746
- [13] Zhang L, Taniguchi S (2000) Fundamentals of inclusion removal from liquid steel by bubble flotation. *Int Mat Rev* 45:59–82
- [14] Nguyen AV, An-Vo D, Tran-Cong T, Evans GM (2016) A review of stochastic description of the turbulence effect on bubble-particle interactions in flotation. *Int J Miner Process* 156:75–86
- [15] Meng J, Tabosa E, Xie WG, Runge K, Bradshaw D, Manlapig E (2016) A review of turbulence measurement techniques for flotation. *Miner Eng* 95:79–95
- [16] Duan HJ, Ren Y, Zhang LF (2019) Inclusion capture probability prediction model for bubble flotation in turbulent steel flow. *Metall Mater Trans B* 50:16–21
- [17] Chang S, Zou ZS, Liu JH, Isac M, Cao XE, Su XF, Guthrie RIL (2021) Study on the slag-metal interfacial behavior under the impact of bubbles in different sizes. *Powder Technol* 387:125–135
- [18] He YJ, Li QL, Liu W (2011) Effect of combined magnetic field on the eliminating inclusions from liquid aluminum alloy. *Mat Lett* 65:1226–1228
- [19] Jiang DC, Qin SQ, Li PT, Shi S, Wen ST, Tan Y (2017) Electromagnetic separation of silicon carbide inclusions with aluminum penetration in silicon by imposition of supersonic frequency magnetic field. *J Clean Product* 145:45–49
- [20] Reza AM, Reza AM, Guthrie RIL, Isac M (2010) Modeling of electromagnetic separation of inclusions from molten metals. *Int J Mech Sci* 52:1107–1114
- [21] Wang SQ, Zhang LF, Tian Y, Li YL, Ling H (2014) Separation of non-metallic inclusions from molten steel using high frequency electromagnetic fields. *Metall Mater Trans B* 45:1915–1935
- [22] Ren YS, Ma WH, Wei KX, Yu WZ, Dai YN, Morita K (2014) Degassing of aluminum alloys via the electromagnetic directional solidification. *Vacuum* 109:82–85
- [23] Duan HJ, Ren Y, Zhang LF (2019) Modeling of turbulent flow around bubbles in molten steel. *Steel Res Int* 90:1800576
- [24] Xu ZM, Li TX, Zhou YH (2007) Continuous removal of nonmetallic inclusions from aluminum melts by means of stationary electromagnetic field and DC current. *Metall Mater Trans A* 38:1104–1110
- [25] Liu XF, Liao WN, Sun JH (2018). Negative pressure continuous casting device and method. CN108817339A.
- [26] Romero JS, Cruchaga MA, Celentano DJ (2013) Evaluation of formation and evolution of microporosity in anodic copper solidification processes: Simulation and experimental validation. *Metall Mater Trans B* 44:624–652
- [27] Liu XF, Liao WN, Yang YH (2020) Thermal characteristics and uniformity of microstructures during temperature controlled mold continuous casting profiled copper alloy strip. *Int Commun Heat Mass Transf* 110:104414
- [28] Yang YH, Liu XF, Wang SQ (2020) Thermal characteristics of induction heating with stepped diameter mold during two-phase zone continuous casting high-strength aluminum alloys. *Int Commun Heat Mass Transf* 152:119479
- [29] Buliński P, Smolka J, Siwiec G et al (2019) Numerical examination of the evaporation process within a vacuum induction furnace with a comparison to experimental results. *Appl Therm Eng* 150:348–358
- [30] Yang YH, Chen RR, Guo JJ, Ding HS, Su YQ (2018) Numerical analysis for electromagnetic field influence on heat transfer behaviors in cold crucible used for directional solidification. *Int Commun Heat Mass Transf* 122:1128–1137
- [31] Ebrahimi M, Crapper M (2017) CFD-DEM simulation of turbulence modulation in horizontal pneumatic conveying. *Particuology* 31:15–24

- [32] Geng SN, Yang W, Jiang P, Han C, Ren LY (2022) Numerical study of keyhole dynamics and porosity formation during high-power oscillating laser welding of medium-thick aluminum alloy plates. *Int J Heat Mass Transf* 194:123084
- [33] Chattopadhyay K, Isac M, Guthrie RIL (2011) Considerations in using the discrete phase model (DPM). *Steel Res Int* 82:1287–1289
- [34] Joachim H, Manfred Z, Andreas A, Werner O (2005) Optimization of the tundish design to increase the product quality by means of numerical fluid dynamics. *Steel Res Int* 76:59–63
- [35] Chen C, Ni PY, Jonsson LTI, Tilliander A, Cheng GG, Jönsson PG (2016) A model study of inclusions deposition, macroscopic transport, and dynamic removal at steel-slag interface for different tundish designs. *Metall Mater Trans B* 47:1916–1932
- [36] Choi JI, Park Y, Kwon O, Lee C (2016) Interparticle collision mechanism in turbulence. *Phys Rev E* 93:13112
- [37] Picardo JR, Agasthya L, Govindarajan R, Ray SS (2019) Flow structures govern particle collisions in turbulence. *Phys Rev Fluid* 4:32601
- [38] Kruis FE, Kusters KA (1997) The collision rate of particles in turbulent flow. *Chem Eng Commun* 158:201–230
- [39] Lindborg U, Torssell K (1968) A collision model for the growth and separation of deoxidation products. *Trans Metall Soc* 242:94–109
- [40] Cai H, Sun CC, Miao GQ (2021) The Bernoulli effect in horizontal granular flows. *Soft Matter* 17:1839–1845
- [41] Qin RQ, Duan CY (2017) The principle and applications of Bernoulli equation. *J Phys Conf Ser* 916:12038
- [42] Chen SY, Chen XH, Wan DD, Sun X, Ji L, Wu K, Wang GC (2020) Particle-resolved direct numerical simulation of collisions of bidisperse inertial particles in a homogeneous isotropic turbulence. *Powder Technol* 376:72–79

Publisher's Note Springer Nature remains neutral with regard to jurisdictional claims in published maps and institutional affiliations.

Springer Nature or its licensor (e.g. a society or other partner) holds exclusive rights to this article under a publishing agreement with the author(s) or other rightsholder(s); author self-archiving of the accepted manuscript version of this article is solely governed by the terms of such publishing agreement and applicable law.